Petroleum Science 23 (2026) 4296–4319

Contents lists available at ScienceDirect

Petroleum Science

journal homepage: www.keaipublishing.com/en/journals/petroleum-science

Original Paper

Investigation of tip leakage vortex instability and pressure pulsation characteristics in a vane-type multiphase pump

Hai-Gang Wen [a,b], Guang-Tai Shi [a,b,*], Wen-Juan Lv [a,b], Hao Qin [a,b]

[a] School of Energy and Power Engineering, Xihua University, Chengdu, 610039, Sichuan, China
[b] Key Laboratory of Fluid and Power Machinery (Xihua University), Ministry of Education, Chengdu, 610039, Sichuan, China

ARTICLE INFO

Article history:
Received 4 September 2025
Received in revised form
5 November 2025
Accepted 17 April 2026
Available online 22 April 2026

Edited by Min Li

Keywords:
Vane-type multiphase pump
Gas-liquid two-phase flow
Vortex evolution
Pressure pulsation
Experimental measurements
Computational fluid dynamics

ABSTRACT

As a key efficient transportation equipment in oil-gas extraction, vane-type multiphase pumps face significant performance limitations due to extensive vortex formation in flow channels. This study systematically investigates strong-weak vortex evolution in impellers using vorticity decomposition, secondary flow diagnosis, and rigid vorticity vector analysis. It examines how inlet gas volume fraction and flow rate affect axial vortices, circumferential vortices, and pressure pulsation. Key findings include: 1) Tip leakage vortex (TLV) in these pumps demonstrates fracture zones, leading to a proposed "front-middle-rear leakage vortex" structure; 2) TLV diffusion and shedding represent strong-weak vortex transitions, with mutual compression between front and middle vortices directly causing fracture; 3) Blade geometry correlates with fluid potential rotor enthalpy evolution to predict vortex patterns; 4) Circumferential vortex intensity increases with gas accumulation, while rapid axial vortex development influences gas distribution. Time-frequency analysis shows gas phase presence amplifies pressure pulsation and low-frequency disturbances in TLV regions, with axial vortex proliferation being the primary contributor to enhanced pulsation intensity. High-flow conditions intensify peripheral pulsations through unbroken TLV, while reduced front leakage vortex and rear vortex shedding attenuate pressure fluctuations.

© 2026 Publishing services by Elsevier B.V. on behalf of KeAi Communications Co. Ltd. This is an open access article under the CC BY-NC-ND license (http://creativecommons.org/licenses/by-nc-nd/4.0/).

1. Introduction

The global coastline and vast land areas are rich in oil and natural gas resources, making their efficient extraction an urgent priority. However, extracting these resources from deep-sea and inland underground locations is challenging and time-consuming. Selecting appropriate extraction and transportation equipment can significantly improve efficiency. Current equipment mainly includes screw pumps (Cao et al., 1999) and vane-type multiphase pumps (Cheng and Chen, 1999; Ling, 2000). Compared to conventional screw pumps, vane-type multiphase pumps offer advantages such as longer service life, easier maintenance, and higher transportation capacity. In particular, enclosed gathering and transportation technology has greatly simplified the transportation process, effectively reducing maintenance costs. The research and design of vane-type multiphase pumps have long been a focal point of study worldwide. Over the past decade, continuous optimization and improvements by researchers have led to significant performance enhancements (Yao et al., 2020).

However, there remain numerous challenges to be addressed in the practical operation of vane-type multiphase pumps, particularly the large-scale vortices that form in the flow channels of the pressure-boosting unit, which significantly impact pump performance (Zhang et al., 2014; Li et al., 2013; Ling, 2000). In a vane-type multiphase pump, the impeller is a rotating component, and there must be a certain gap between the blade tip and the inner wall, known as the tip clearance. The fluid leaking through this gap forms a jet driven by the pressure difference on both sides of the blade, which then interacts with the main flow and evolves into a TLV. The TLV not only intensifies unstable flow within the pump but also induces hazards such as cavitation, vibration, and noise. Additionally, secondary flows and leakage vortices in the flow channels collide, merge, and dissipate, leading to significant energy losses and further reducing the pump's work capacity and efficiency. Meanwhile, vortex-induced disturbances generate

* Corresponding author.
E-mail address: sgtaixh@mail.xhu.edu.cn (G.-T. Shi).
Peer review under the responsibility of China University of Petroleum (Beijing).

https://doi.org/10.1016/j.petsci.2026.04.031
1995-8226/© 2026 Publishing services by Elsevier B.V. on behalf of KeAi Communications Co. Ltd. This is an open access article under the CC BY-NC-ND license (http://creativecommons.org/licenses/by-nc-nd/4.0/).

(a) Impeller **(b)** Guide vane **(c)** Pump casing

Fig. 6. The physical components of the pressure-boosting unit in the multiphase pump.

Fig. 7. Experimental test system (left) and high-speed camera setup (right).

the underlying mechanisms of leakage vortex "instability-fragmentation-shedding" through SVF/WVF analysis.

Fig. 13 shows the vortex distribution in the vane-type multiphase pump under pure water conditions, including SVF, Middle Vortex Flow (MVF), and WVF. To facilitate the investigation of leakage vortex trajectories, ten vortex core points (P_1–P_{10}) were extracted along the vortex axis. As shown in Fig. 14, the front and main leakage vortices primarily consist of SVF, whereas the rear leakage vortex is mainly composed of WVF.

In the pump flow passage, a low peak of rigid vorticity appears at the junction between the front and main leakage vortices. Theoretically, this region is prone to vortex dissipation and is therefore identified as the first breakage point of the leakage vortex. In the rear leakage vortex region, significant vortex shedding is observed, with the presence of gas phase notably amplifying the shedding scale. Consequently, the leakage vortex exhibits two primary dissipation zones, both predominantly consisting of WVF.

To further reveal the intrinsic causes of flow instability in the vane-type multiphase pump, a direct comparison was made between the circumferential velocity and vortex distribution at vortex core points. Fig. 15 shows the circumferential velocity distribution of leakage vortices and vortex cores under pure water conditions.

From Fig. 15(a), it is observed that from P_1 to P_5, as the SVF decreases, the circumferential velocity along the vortex axis gradually declines, particularly reaching a low peak at point P_5. This region primarily consists of WVF and corresponds to the first instability zone of the leakage vortex. A similar trend is observed in the P_5–P_{10} range, where the circumferential velocity at vortex core

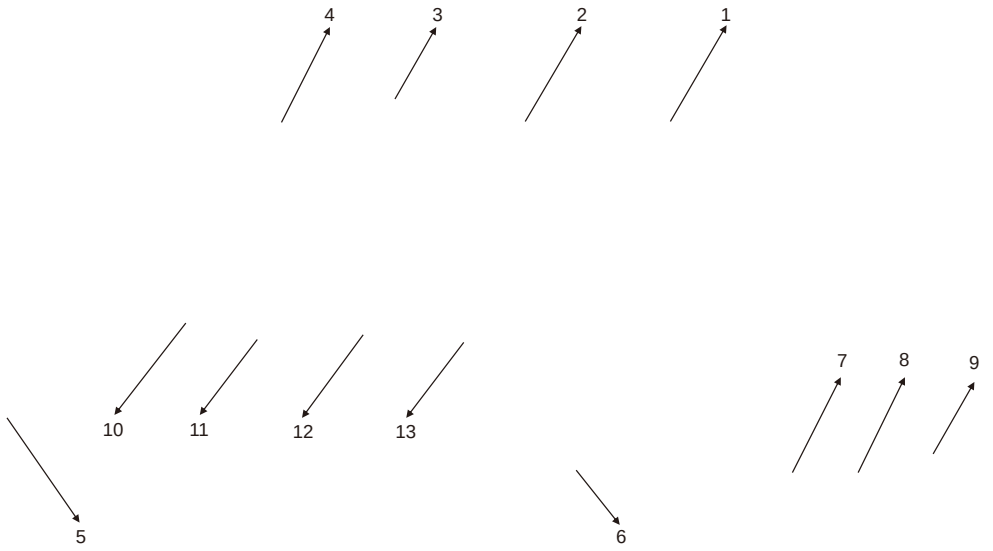

Fig. 8. Schematic diagram of the experimental system for the multiphase pump. 1: Water tank; 2: regulating valve; 3: booster pump; 4: flow meter; 5: gas–liquid mixing tank; 6: pressure sensor; 7: multiphase pump; 8: torque meter; 9: electric machine; 10: gas flow meter; 11: regulating valve; 12: gas pressure meter; 13: air compressor.

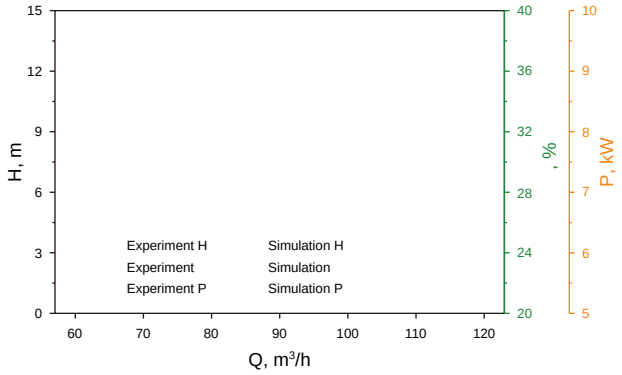

Fig. 9. Comparison of the results of tests and numerical simulations.

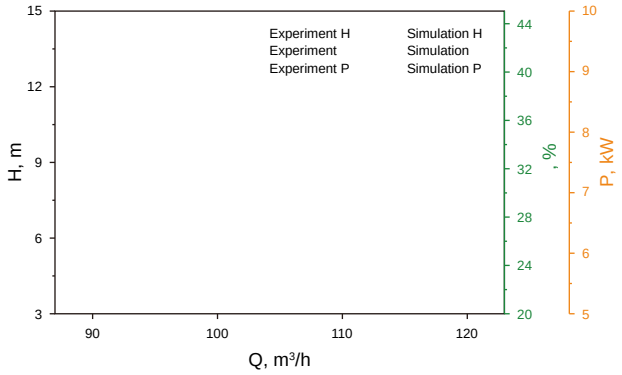

Fig. 10. Comparison of experimental and numerical simulation under gas–liquid two-phase conditions.

points exhibits a positive correlation with the SVF magnitude. Fig. 15(b) reveals that the MVF significantly increases in the front and main leakage vortex regions. The presence of the gas phase reduces the circumferential velocity along the vortex axis, and this localized decrease in circumferential velocity promotes stable vortex growth—especially the noticeable expansion of WVF scales.

Fig. 11. Distribution of TLV (IGVF ˆ 10%).

Fig. 12. Vortex breakage region (experimental visualization).

Fig. 13. Diffusion effects of TLV.

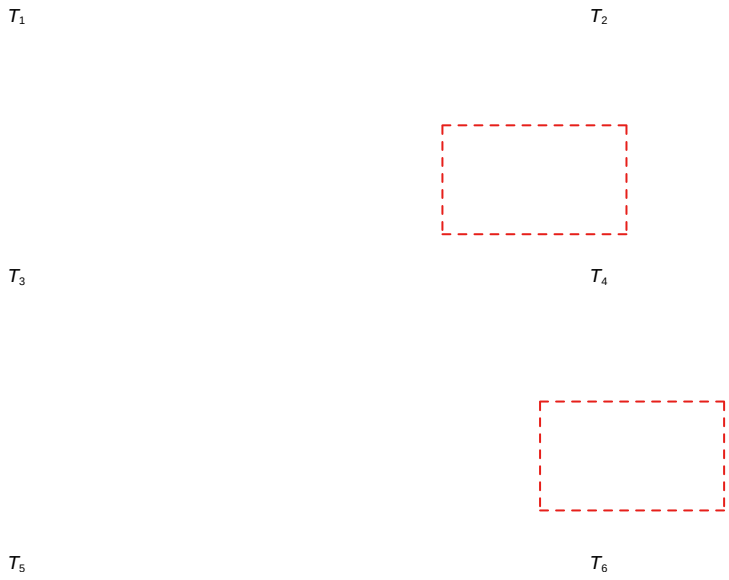

Fig. 17. High-speed photographic sequence of TLV breakage region evolution (IGVF ˆ 10%).

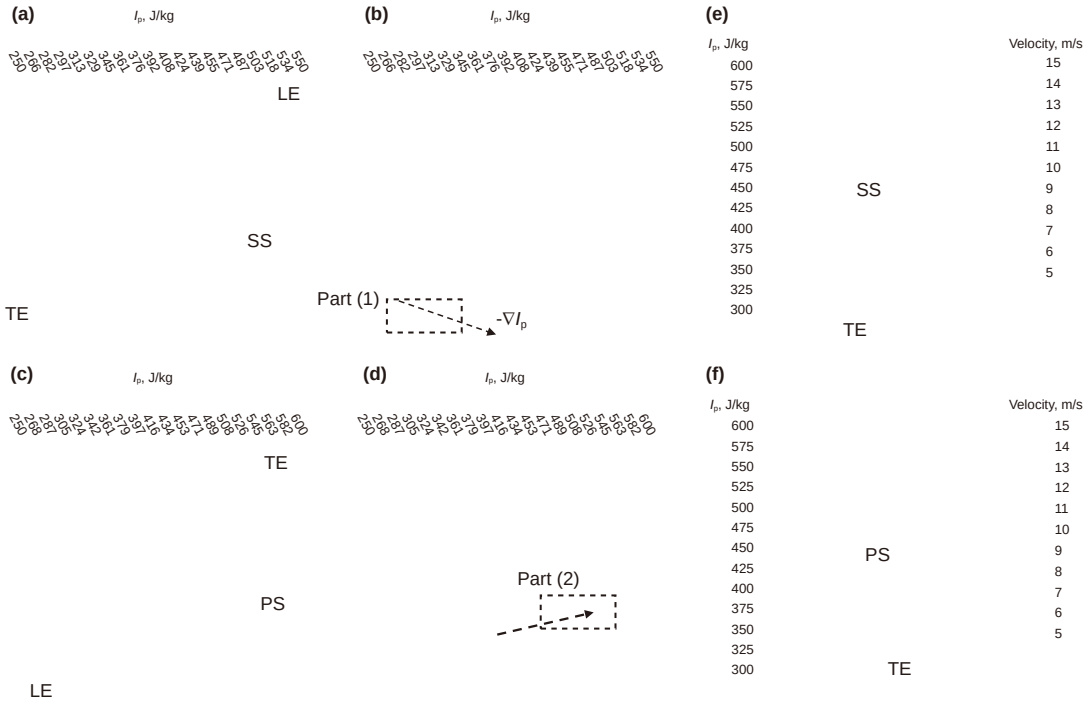

Fig. 18. PRG distribution on impeller blade surfaces: (**a**) Pressure surface (PS), IGVF ˆ 0%; (**b**) Pressure surface, IGVF ˆ 10%; (**c**) Suction surface (SS), IGVF ˆ 10%; (**d**) Suction surface, IGVF ˆ 10%; (**e**) Enlarge of Part (1); (**f**) Enlarge of Part (2).

suction and pressure sides significantly deviate from the blade profile—a key factor in vortex destabilization. Fig. 19(a) and (b) show that the initiation point of the front leakage vortex coincides with the suction-side leading edge, aligning precisely with the onset of I_p contour deviation and a locally high potential rothalpy gradient. Elsewhere along the leading edge, well-distributed I_p

contours correlate with minimal vortex activity, demonstrating effective flow control through blade profile design.

Fig. 19(c) and (d) reveal severe I_p contour distortion near the pressure side, spatially coinciding with the main leakage vortex. As the tip-region I_p contours progressively deviate from the blade geometry, the leakage vortex forms and diffuses into the passage. Conversely, when I_p contours realign parallel to the blade profile in the rear section, the vortex dissipates into fine-scale turbulent structures.

Fig. 20 displays the transient evolution of leakage vortices and SI values (ratio of PRG to Coriolis force, directly indicating flow stability) under pure water conditions. The SI distribution on blade surfaces synchronizes with vortex spatiotemporal evolution. During 0.414–0.42 s (vortex growth phase), the main leakage vortex expands while adjacent blades exhibit rising SI values, both propagating toward the outlet. By T ˆ 0.42 s, the rear leakage vortex evolves into a spiral pattern in the passage rear section. Under gas-liquid conditions, the leading-edge suction side shows intensified leakage vortices and SI values. Gas phase enlarges inlet instability zones, amplifies vortex scales, and accelerates diffusion—evidenced by prominent vortex shedding at T ˆ 0.42 s. Despite gas-induced secondary flow enhancement, the blade rear section maintains stable SI values, proving that the long-wrap-angle helical blades effectively adapt to multiphase flows by suppressing vortex diffusion at design conditions.

5.3. Influence of gas volume fraction on flow characteristics and hydraulic performance

Fig. 21 presents the average distributions of turbulent dissipation rate, potential rothalpy gradient, and pressure boost values across the pump's inlet/outlet under varying gas volume fractions (IGVF). The data reveal that as IGVF increases from 0% to 20%, turbulent dissipation rate surges from 2332 to 7965 m^2/s^3, pressure boost declines from 80,640 to 56,135 Pa. A sharp rise in PRG occurs beyond 10% IGVF, accompanied by rapid deterioration of pressure-boosting performance. The most pronounced changes in turbulent dissipation, potential rothalpy gradient, and pressure differential emerge during the 15%–20% IGVF transition. These trends demonstrate that rising gas content intensifies flow instability, elevating turbulent dissipation and energy losses while degrading pressure-boosting capacity.

Fig. 22 shows the distribution of SI values at the impeller and guide vane outlets under different flow rates at IGVF ˆ 10%. It can be observed from Fig. 22 that as the flow rate increases from 0.6Q to 1.0Q, the SI value at the impeller outlet of the vane-type multiphase pump decreases from 0.98 to 0.58, indicating a gradual reduction in overall secondary flow within the passage. At the low flow rate of 0.6Q, the average SI value at the impeller outlet approaches 1, suggesting poor flow uniformity under extreme operating conditions, which readily induces unstable vortices such

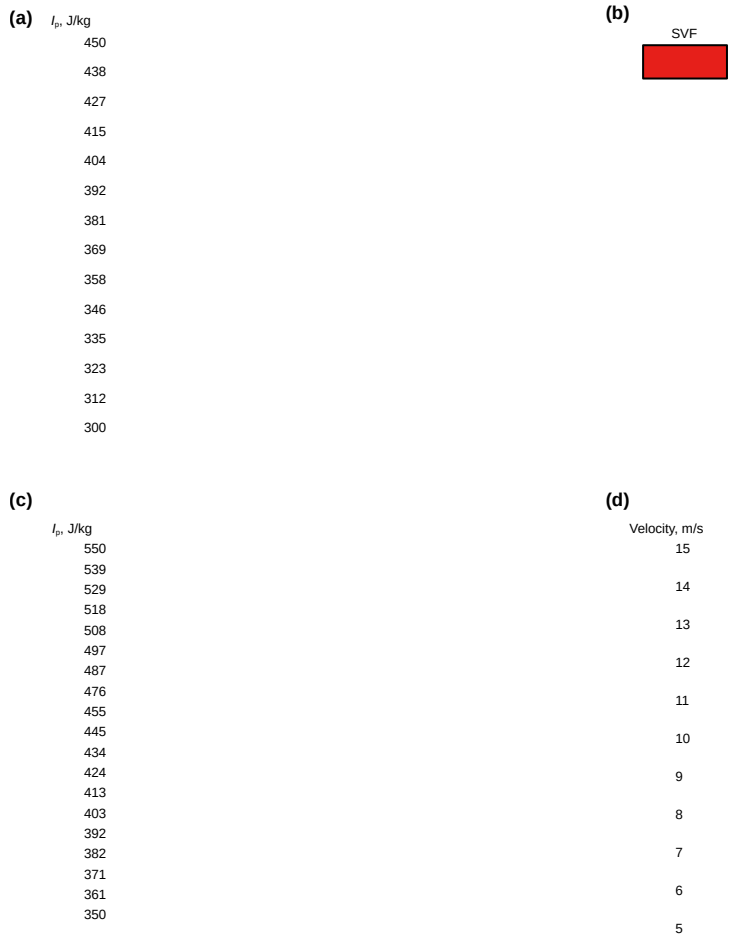

Fig. 19. TLV and PRG characteristic distributions (IGVF ˆ 10%): (**a**) Distribution of the I_p; (**b**) F-TLV; (**c**) Distribution of the I_p; (**d**) Streamline of the M-TLV and the B-TLV.

Fig. 20. Transient evolution of leakage vortex and stability index (SI) under two-phase conditions: (**a**) Pure water; (**b**) IGVF ˆ 10%.

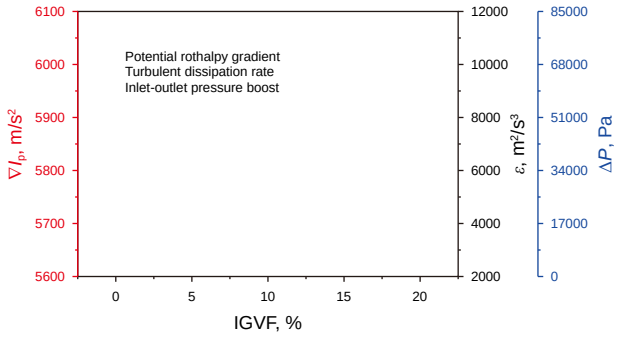

Fig. 21. Distributions of potential rothalpy gradient, turbulent dissipation rate, and pressure boost at pump inlet/outlet.

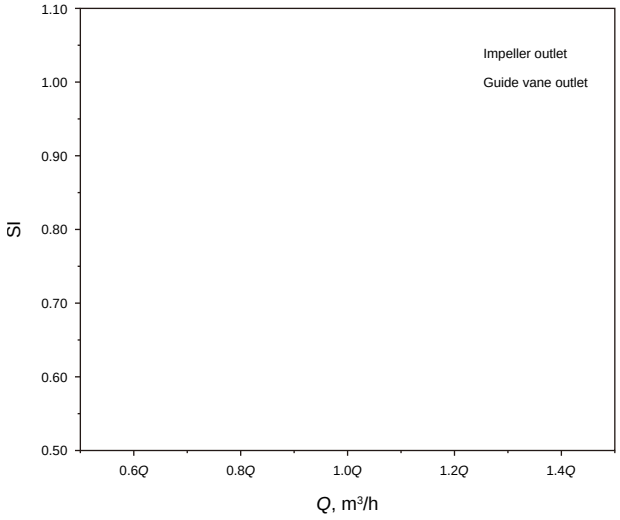

Fig. 22. SI value distribution at impeller/guide vane outlets under different flow rates.

as secondary flow. Furthermore, as the inlet flow rate increases from 0.6*Q* to 1.0*Q*, the SI value at the impeller outlet gradually decreases to 0.59. At 1.2*Q*, the SI value at the impeller outlet increases to 0.68, while the SI value at the guide vane outlet decreases to 0.52. When the flow rate increases to 1.4*Q*, the SI value at the impeller outlet rises to 0.77, and the SI value at the guide vane outlet increases to 0.6.

It can be seen that the inlet flow rate significantly affects the flow characteristics in the vane-type multiphase pump, and adjusting the flow rate can effectively control the internal flow of hydraulic machinery. In practical operation, the secondary flow diagnostic theory can effectively identify the flow stability state of the vane-type multiphase pump under different operating conditions. It is found that under gas-liquid two-phase conditions, the outflow condition at the design flow rate is relatively the most stable, and the total energy loss at the outlet of the pressure-boosting unit is the lowest. This also provides a more accurate theoretical basis for the optimized operation of the vane-type multiphase pump.

5.4. Vortex decomposition and energy loss in the vane-type multiphase pump

Fig. 23 shows the distribution of axial vortices, circumferential vortices, radial vortices, and tip clearance streamlines under pure water conditions. From Fig. 23, it can be observed that the tip clearance streamlines flow out from the leading edge of the tip clearance and move circumferentially along the passage to the outlet position, forming a long strip of TLV. Among the components of the TLV, the circumferential vortex accounts for the largest proportion compared to the axial and radial vortices, making it the main component of the TLV. At the same time, in the front TLV region, the vortex components are mainly

circumferential vortices, while axial vortices begin to appear in the middle breakage region of the leakage vortex, where the kink degree of the jet streamlines is relatively low. In addition, near the shear band of the leakage vortex, the jet from the adjacent passage flows in through the clearance and intertwines with the main flow, forming the middle part of the leakage vortex. Axial vortices are mainly concentrated near the leading edge of the blade pressure side and the tail region of the leakage vortex. Circumferential vortices account for the largest proportion of the leakage vortex and are therefore the main component, while radial vortices account for the smallest proportion and are mainly distributed in local regions near the leading and trailing edges of the blade. Furthermore, when the fluid passes through the narrowest part of the passage, the axial vortices in the passage are relatively severe. At the same time, when the tail of the leakage vortex experiences flow separation and dissipation, the proportion of the axial component of the vortex is also large, which fully indicates that the axial component plays a certain driving role in the generation and collapse of the vortex.

Fig. 24 shows the distribution of axial vortices, circumferential vortices, radial vortices, and tip clearance streamlines at an inlet gas volume fraction of 10%. From Fig. 24, it can be seen that under gas-liquid two-phase conditions, the leakage jet streamlines are more densely distributed in the passage, and there are relatively fewer jets in the shear band. Near the clearance in the shear band region, obvious gas accumulation occurs, and in most regions near the trailing edge clearance of the blade, the gas volume fraction is very high. It can also be seen from Fig. 24 that compared to the pure water condition, the distribution of axial vortices at the tail of the leakage vortex gradually increases under gas-liquid two-phase conditions, meaning that the axial component gradually increases when the vortex sheds and dissipates. In the front and rear sections of the leakage vortex, the vortex scale of the circumferential vortex is significantly larger, but the vortex intensity of the circumferential vortex begins to decrease in local regions in the middle of the leakage vortex. This is caused by local gas blockage in the clearance, which reduces the velocity of the clearance jet at this position and prevents it from forming strong convection with the main flow on the pressure side, thereby affecting the diffusion of the circumferential vortex to some extent. It can be concluded that axial and circumferential vortices are the main components of the vortex, and the presence of gas significantly increases the distribution of axial and circumferential vortices throughout the impeller region.

The preceding analysis has identified the core positions of tip leakage vortices in the vane-type multiphase pump. The following section will conduct an in-depth analysis of the correlation between energy loss and vortex intensity at the vortex core, with quantitative analysis revealing their relationship patterns.

Fig. 25 shows the distribution of circumferential vortices, axial vortices, and energy loss along the vortex core under 10% gas volume fraction. From Fig. 25, it can be observed that along the vortex axis of the TLV, the variation patterns of rigid vorticity for both circumferential and axial vortices at different spatial positions correspond with energy loss distribution.

In the P_1–P_4 interval, the rigid vorticity of both circumferential and axial vortices gradually decreases from 7844 s^{-1} and 666 s^{-1} to 1187 s^{-1} and 491 s^{-1} respectively, while the entropy production rate at the vortex core correspondingly drops from 13,783 to 4665 W/(m^3·K). During the P_4–P_6 interval, both axial and circumferential vortices at the vortex core begin to increase, with axial vortices showing the most rapid growth. Concurrently, the entropy production rate rises to 18,711 W/(m^3·K), indicating that the axial vortex growth at P_6 contributes significantly to energy loss. Point P_6 is located at the leading edge of the blade suction side, where both axial and circumferential vortices are most densely distributed—the primary reason for its maximum energy loss. In the P_6–P_9 interval, the rigid vorticity of both axial and circumferential vortices gradually decreases, accompanied by a substantial reduction in energy loss. However, from P_9 to P_{10}, as the leakage vortex enters the rear leakage vortex stage, large-scale vortex shedding occurs in the flow passage, leading to significant energy loss and consequent increase in entropy production rate.

5.5. Transient characteristics of TLV and gas phase in vane-type multiphase pump

Fig. 26 shows the distribution of circumferential vortices, axial vortices, and gas phase in the impeller passage under different flow rates at an inlet gas volume fraction of 10%. From Fig. 26, it can be observed that at 0.8Q flow rate, the leading edge of the blade suction side fails to form a stable structure, and the pressure side is dominated by circumferential vortices. The inlet circumferential velocity is relatively low, but vortex and gas phase concentrations increase

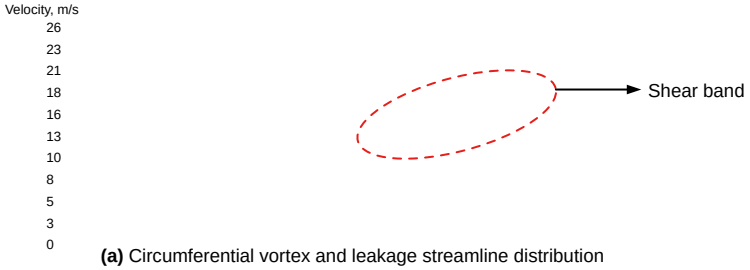

(a) Circumferential vortex and leakage streamline distribution

(b) Radial vortex and leakage streamline distribution

(c) Axial vortex and leakage streamline distribution

Fig. 23. Axial, circumferential, and radial vortices with tip clearance streamlines (IGVF ˆ 0%).

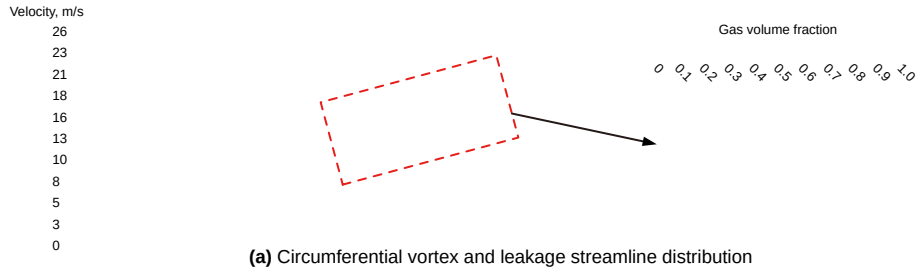

(a) Circumferential vortex and leakage streamline distribution

(b) Radial vortex and leakage streamline distribution

(c) Axial vortex and leakage streamline distribution

Fig. 24. Spatial distribution of axial/circumferential/radial vortices and tip clearance streamlines (IGVF ˆ 10%).

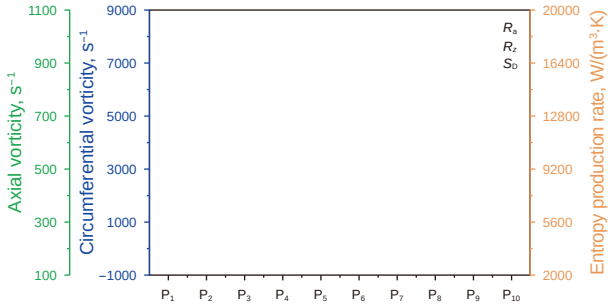

Fig. 25. Circumferential/axial vortices and energy loss along vortex cores.

near the passage outlet. When the flow rate increases to 1.0*Q*, the leakage vortex at the suction side leading edge gradually forms, but breakage occurs near the pressure side leading edge. At this stage, axial vortices become more prominent at the pressure side leading edge and mid-region, while both circumferential and axial velocities increase. Notably, at the passage inlet, the circumferential velocity decreases toward the tip region across all cross-sections. This velocity gradient-induced shear effect significantly enlarges the scale of circumferential vortices. Under 1.2*Q* flow rate, axial vortices in the passage gradually diminish, and the distribution of circumferential vortices shifts toward the suction side. Concurrently, the leakage vortex no longer exhibits significant breakage, and the circumferential vortices near the pressure side leading edge closely approach the suction side of adjacent blades.

The above analysis reveals that at low flow rates, circumferential and axial vortices are constrained by the shear effects of circumferential and axial velocities, resulting in smaller vortex scales of the leakage vortex, with distribution limited to the vicinity of the blade pressure side leading edge. At the design flow rate, the distribution of axial vortices gradually increases in the tail region of the leakage vortex, while circumferential vortices become significantly more concentrated near the suction side leading edge. However, distinct breakage and instability zones emerge under these conditions. At high flow rates, the inlet velocity increases, but the circumferential velocity variation near the suction side leading edge remains minimal. The initiation position of the leakage vortex shifts downward, with circumferential vortices predominantly distributed along the suction side, effectively preventing breakage in the mid-region of the leakage vortex.

These findings demonstrate that flow rate significantly influences vortex distribution and gas-liquid separation characteristics. At low flow rates, the TLV remains relatively small, whereas at design and high flow rates, the TLV becomes more pronounced. Furthermore, the degree of gas phase accumulation in the flow passage is strongly affected by vortex behavior. Therefore, this section focuses on analyzing the transient evolution of the TLV and gas phase at design and high flow rates.

Fig. 27 illustrates the three-dimensional spatiotemporal evolution of vortices and the gas phase at a flow rate of 1.0*Q*. From Fig. 27, it can be observed that at 1.0*Q*, the distribution of circumferential vortices in the impeller passage aligns with the gas phase at different time instants. At 0.4131 s, circumferential vortices form near the blade suction side, while axial vortices, radial vortices, and gas phase distribution remain minimal. By 0.4164 s, the circumferential vortices gradually shift toward the pressure side, and the vortex regions of the front and middle leakage vortices begin compressing toward the mid-region, forming a breakage zone. The vortex axis in the circumferential direction moves in opposite directions, ultimately leading to breakage at 0.42 s.

During the period T ˆ [0.4131 s, 0.42 s], axial vortices diffuse from the leading edge toward the outlet. As the breakage zone develops, both circumferential and axial vortices progressively increase in the flow passage, accompanied by a growing concentration of gas phase within the vortices. This indicates that vortex diffusion and growth intensify gas phase accumulation in the passage.

Fig. 28 shows the three-dimensional spatiotemporal evolution of vortices and gas phase at a flow rate of 1.2*Q*. From Fig. 28, it can be observed that compared to the 1.0*Q* flow rate, the variation of vortices in the flow passage over time is smaller at 1.2*Q*. The initial position of circumferential vortices is relatively delayed. During the period T ˆ [0.4131 s, 0.4164 s], circumferential vortices gradually diffuse toward the middle of the flow passage, with their scale significantly increasing. Meanwhile, the gas phase exhibits a tubular distribution and is entrained by the vortices toward the outlet. At 0.42 s, the scale of circumferential vortices gradually decreases, and the distribution area of the gas phase also reduces. However, the structure of the TLV remains stable without breakage. Fig. 28 also reveals that at 1.2*Q* flow rate, axial vortices are less distributed, and

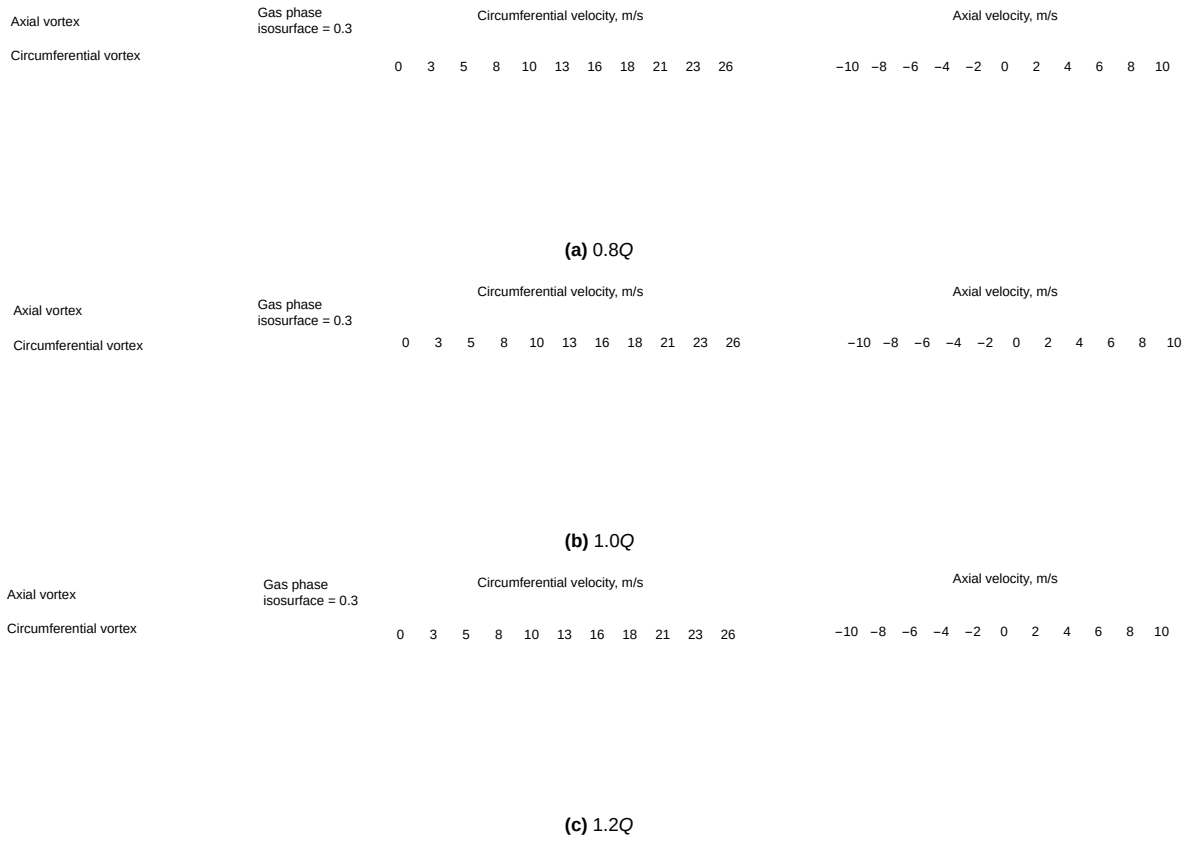

Fig. 26. Distributions of circumferential/axial vortices and gas phase (IGVF ˆ 10%).

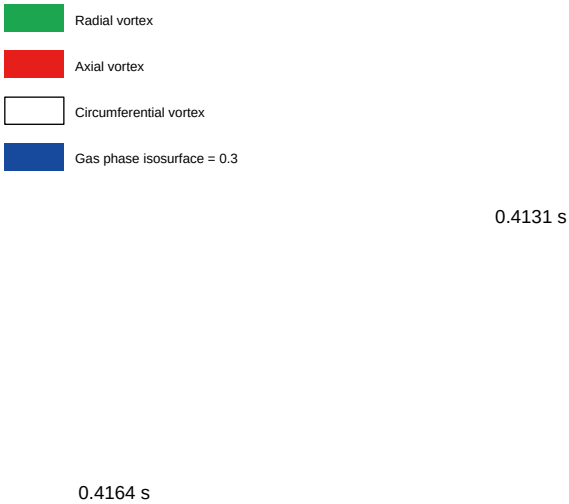

Fig. 27. 3D spatiotemporal evolution of vortices and gas phase at 1.0*Q* flow rate (IGVF ˆ 10%).

their increase is slow during T ˆ [0.4131 s, 0.42 s]. Circumferential vortices exhibit an elongated distribution, and vortex shedding in the rear leakage vortex region is minimal, which is related to the slower development of axial vortices in the flow passage.

In summary, as the inlet flow rate increases, both the circumferential and axial velocities in the shroud region of the flow passage also increase, thereby influencing the positional changes of the TLV. The continuous dissipation and regeneration of axial and circumferential vortices over time further entrain the gas phase toward the outlet, demonstrating that the spatiotemporal evolution characteristics of vortices significantly affect gas-liquid two-phase transport.

5.6. Pressure pulsation characteristics in vane-type multiphase pump

In studies concerning pressure pulsations in vane-type multiphase pumps, Wen et al. (2022) found a strong correlation between

tip leakage vortices and pressure pulsations. Therefore, the following analysis takes monitoring points at the core positions of tip leakage vortices at different locations to examine the relationship between pressure pulsations and circumferential/axial vortices.

Fig. 29 shows monitoring points (IM1~IM5) in the core region of the TLV under one operating condition. These points will vary with changes in the vortex core center under different conditions. All five points are located along the vortex axis of the TLV, with IM2 in the front leakage vortex region, IM3-IM4 in the middle leakage vortex region, and IM5 in the rear leakage vortex region. This section conducts an in-depth analysis of pressure pulsations at these five points to reveal patterns in frequency and time domain variations under different operating conditions.

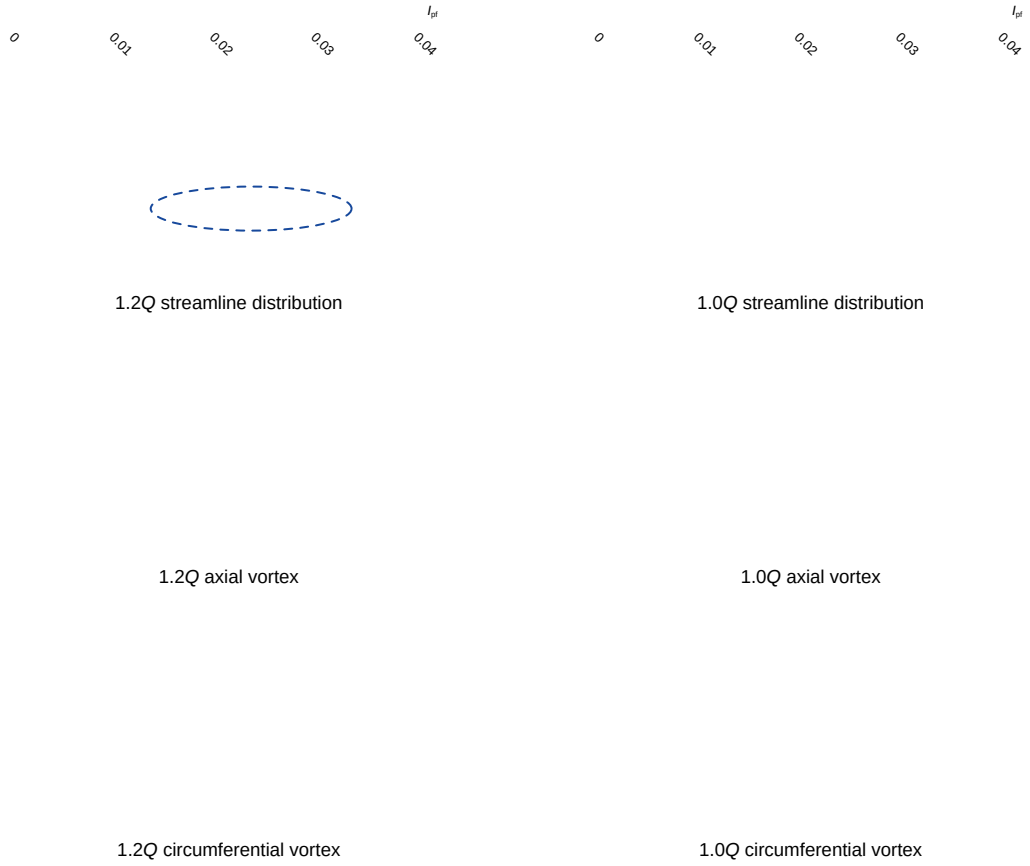

Fig. 35. Vortex/streamline/pressure pulsation intensity distributions at different flow rates.

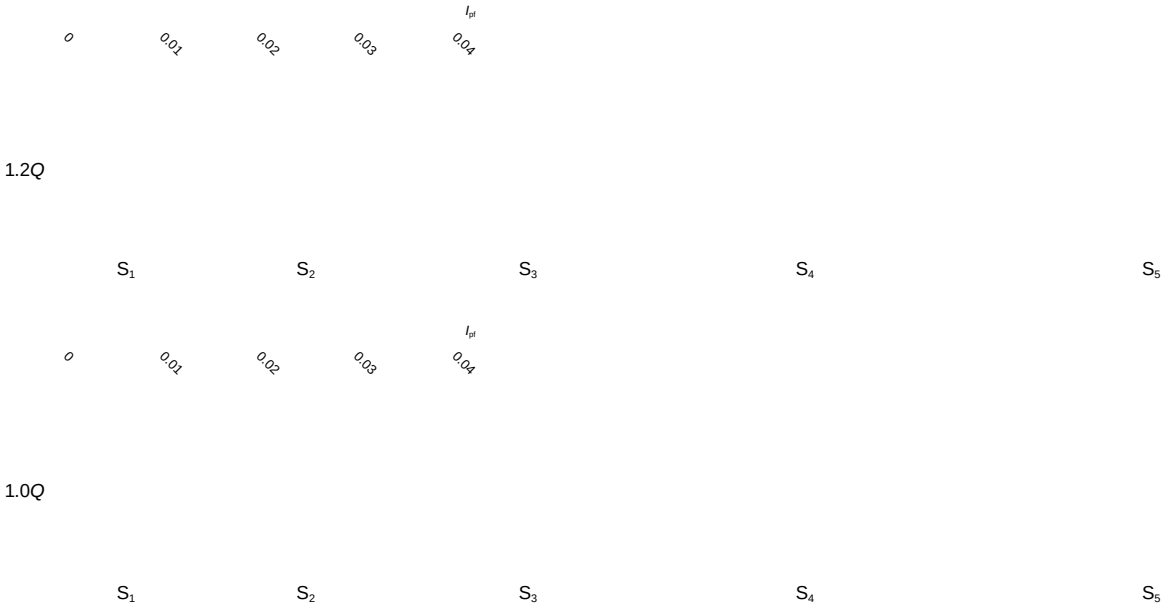

Fig. 36. Pressure pulsation intensity distributions at cross-sections under different flow rates (IGVF ˆ 10%).

This indicates that at low flow rates, the dominant and secondary frequencies at all five monitoring points are below 19 times the rotational frequency, and their amplitudes are notably lower than those under the other two flow conditions except for IM1, which is closely related to the distribution of leakage vortices in the impeller passage. Under low flow conditions, the pressure amplitudes near the suction side inlet of the impeller are higher and concentrated in low frequencies, which can cause significant

damage to the vane-type multiphase pump. As the inlet flow rate increases, the pressure pulsation amplitudes at the suction side inlet gradually decrease.

Fig. 33 also reveals that at 0.8*Q*, the pressure pulsation amplitudes at the dominant frequencies of the other four points (excluding IM1) are generally low, which is associated with the reduced presence of tip leakage vortices in the flow passage. In contrast, at 1.0*Q* and 1.2*Q*, the pressure pulsation amplitudes are higher and concentrated in regions with dense leakage vortex distributions, demonstrating an inseparable link between vortex distribution and pressure pulsations. Adjusting the flow rate to control tip leakage vortices, thereby reducing pressure pulsations in the flow passage, provides valuable guidance for improving the performance of multiphase pumps.

In summary, under off-design operating conditions, pressure pulsations at the core of the TLV are mostly concentrated in low frequencies with smaller amplitudes at low flow rates, whereas at high flow rates, local regions exhibit larger low-frequency pressure pulsation amplitudes. This phenomenon is strongly correlated with the evolution and distribution of leakage vortices.

5.7. Correlation between TLV and pressure pulsation intensity

Fig. 34 shows the distribution of tip leakage vortices and pressure pulsation intensity under gas-liquid two-phase conditions. From Fig. 34, it can be observed that during the front leakage vortex stage, the distribution of pressure pulsation intensity aligns with that of circumferential vortices. At the impeller inlet, the TLV primarily consists of circumferential vortices, which exhibit an elongated distribution, while axial vortices appear as fragmented strips. From cross-section S_2 to S_3, as axial vortices emerge, the pressure pulsation intensity eventually forms two concentrated regions at cross-section S_3. The high-pressure pulsation region gradually expands along the flow direction, primarily due to the increasing scale of circumferential vortices. This expansion is closely linked to the growth of vortex structures and their interaction with the surrounding flow field. The results highlight the significant influence of circumferential vortices on pressure pulsation characteristics in multiphase pumping systems.

Fig. 34 further reveals that during the middle leakage vortex stage, both circumferential and axial vortices coexist. Here, circumferential vortices concentrate near the shroud, entraining the medium toward the outlet. At cross-section S_5, the scale of axial vortices begins to increase, accompanied by an expansion of high-pressure pulsation intensity regions, which are distributed closer to the hub.

At cross-section S_6, the TLV appears in a shedding form. In this region, circumferential vortices gradually decrease while axial vortices increase in both distribution and volume. Concurrently, pressure pulsations intensify in the terminal region of the middle leakage vortex, exhibiting a diffusion trend consistent with axial vortices. Under conditions of 1.0*Q* flow rate and 10% inlet gas volume fraction, the growth of axial vortices indicates vortex shedding in this area. Such shedding exacerbates secondary flow disturbances and further influences pressure pulsation variations.

The analysis demonstrates that different vortex types dominate pressure pulsation intensity at various locations in the vane-type multiphase pump impeller. The front leakage vortex region is primarily influenced by circumferential vortices driving pressure pulsation changes, while the middle leakage vortex region is mainly affected by axial vortices causing pressure pulsation variations.

Fig. 35 displays the distribution of vortices, streamlines, and pressure pulsation intensity under different flow rates at 10% gas volume fraction. At 1.2*Q* flow rate, the tip leakage streamlines concentrate along the mid-section of the blade suction side. Compared to the design flow rate, pressure pulsation intensity is notably lower during the front leakage vortex stage. In the middle leakage vortex section, however, the pressure intensity of clearance streamlines remains significantly high. Axial and circumferential vortices in Part I show distinct behavior: axial vortices reduce substantially at high flow rates, while circumferential vortices maintain structural integrity without breakage—key factors underlying the region's pronounced pressure pulsation intensity. Conversely, at the design flow rate, pressure pulsation intensity peaks at both the front and rear sections of the leakage vortex. The front section shows dominance of circumferential vortex components, while the rear section experiences large-scale vortex shedding with dramatically multiplied axial vortices. These findings underscore how flow rate modulates vortex morphology and its cascading effects on pressure pulsation characteristics, providing critical insights for operational optimization of multiphase pumps.

Fig. 36 shows the distribution of pressure pulsation intensity at various cross-sections within the impeller passage under different flow rates. From Fig. 36, it can be observed that at high flow rates, the pressure pulsation intensity from cross-section S_1 to S_3 is lower than that at the design flow rate. At cross-section S_4, the pressure pulsation intensity concentrates near the shroud in the middle of the flow passage, where it increases due to vortex influence. At cross-section S_5 under high flow conditions, the concentrated region of pressure pulsation intensity shrinks from circular to small patches and distributes near the blade tip. Combined with Fig. 35, it is evident that this region has fewer axial vortices and less vortex shedding.

In summary, when both axial and circumferential vortices increase simultaneously, the pressure pulsation intensity rises. Adjusting the flow rate can effectively control vortex intensity, thereby reducing pressure pulsation intensity in localized regions.

6. Conclusions

(1) In vane-type multiphase pumps, the TLV breaks into segments at design flow rates, forming front, middle, and rear leakage vortices. Vortex strength weakens along the core path and dissipates through shedding. Circumferential velocity governs both vortex instability and strong-weak transition during development.

(2) At 10% gas content, mutual compression between strong vortices causes leakage vortex breakage. The blade pressure side shows higher potential rothalpy gradients, triggering limited secondary flows. Increasing gas content (0–20%) raises turbulent dissipation but reduces pressure boost. Flow rate changes (0.6*Q*–1.4*Q*) cause SI values at outlets to first drop then rise, with poor flow uniformity under off-design conditions.

(3) Under pure water, axial and circumferential vortices dominate, with circumferential vortices being primary in leakage structures. Both correlate with energy loss. Gas presence intensifies both vortex types, especially axial vortices near the pressure side leading edge, causing significant energy loss. Higher flow rates amplify velocity gradients, altering vortex evolution. Circumferential vortex strength increases with gas accumulation, while axial vortex development affects gas distribution.

(4) Gas-liquid operation generates stronger low-frequency pressure pulsation at vortex cores than pure water. Pulsation patterns vary with flow rates: low rates yield smaller amplitudes, while high rates enhance pulsation in middle leakage regions. Circumferential vortices dominate front leakage pulsation, while axial vortices control middle

leakage pulsation. High flow rates reduce pulsation in front/rear regions due to fewer vortices and suppressed shedding, except where unbroken vortices persist.

CRediT authorship contribution statement

Hai-Gang Wen: Writing – review & editing, Writing – original draft, Validation, Supervision. **Guang-Tai Shi:** Project administration, Funding acquisition. **Wen-Juan Lv:** Writing – original draft, Supervision, Formal analysis, Conceptualization. **Hao Qin:** Investigation, Data curation.

Declaration of competing interest

The authors declare that they have no known competing financial interests or personal relationships that could have appeared to influence the work reported in this paper.

Acknowledgments

The authors acknowledge financial support from the Sichuan Natural Science Foundation Outstanding Youth Science Foundation (2024NSFJQ0012), Key project of Regional Innovation and Development Joint Fund of National Natural Science Foundation of China (U23A20669), Sichuan Science and Technology Program (2022ZDZX0041).

Nomenclature

ρ	Density of the medium, kg/m^3
p	Pressure, Pa
t	Time, s
V	Velocity vector, m/s
u_i	Velocity components in the x, y, and z directions, m/s
u_j	Velocity components in the x, y, and z directions, m/s
f_i	Body force term
μ	Dynamic viscosity, Pa□s
I	Total rothalpy, m^2/s^2
I_p	Potential rothalpy, m^2/s^2
I_k	Kinetic rothalpy, m^2/s^2
ω_i	Impeller angular velocity, rad/s
Q_r	Second invariant of the velocity gradient tensor, s ^{2}
ω_R	Rigid vorticity, s ^{1}
Ω_R	relative vortex intensity, s ^{1}
λ_{ci}	Imaginary part of the complex conjugate eigenvalues of the velocity gradient tensor, s ^{1}
ω	Vorticity vector, s ^{1}
r	Vortex axis direction
C_p	Pressure coefficient
P_i	Instantaneous pressure, Pa
$\overline{P}$	Time-averaged pressure, Pa
U_{tip}	Impeller inlet velocity, m/s
I_{pf}	Pressure pulsation intensity

Subscript

TLV	Tip leakage vortex
PRG	Potential rothalpy gradient
DNS	Direct numerical simulation
RANS	Reynolds-averaged Navier-Stokes

References

Cao, F., Shu, P.C., Xing, Z.W., 1999. Advance in study of twin-screw type multiphase pump. China Petrol. Machin. 27 (3), 49–52. https://doi.org/10.3969/j.issn.1001-4578.1999.03.017 (in Chinese).

Cheng, L.X., Chen, T.K., 1999. Performance and research status of multiphase flow mixed-transport pumps. Oil Field Equip. 28 (5), 22–25. https://doi.org/10.3969/j.issn.1001-3482.1999.05.006 (in Chinese).

Cui, B.L., Zhang, C.L., Zhang, Y.L., et al., 2020. Influence of cutting angle of blade trailing edge on unsteady flow in a centrifugal pump under off-design conditions. Appl. Sci. 10 (2), 580. https://doi.org/10.3390/app10020580.

Dong, X.R., Gao, Y.S., Liu, C.Q., 2019. New normalized rortex/vortex identification method. Phys. Fluids 31 (1), 11701. https://doi.org/10.1063/1.5066016.

Feng, J.J., Luo, X.Q., Guo, P.C., et al., 2016. Influence of tip clearance on pressure fluctuations in an axial flow pump. J. Mech. Sci. Technol. 30 (4), 1603–1610. https://doi.org/10.1007/s12206-016-0315-2.

Furukawa, M., Inoue, M., Saiki, K., et al., 1999. The role of tip leakage vortex breakdown in compressor rotor aerodynamics. J. Turbomach. 121 (3), 469–480. https://doi.org/10.1115/1.2841339.

Gao, Y.S., Liu, J.M., Yu, Y.F., et al., 2019. A Liutex based definition and identification of vortex core center lines. J. Hydrodyn. 31 (3), 445–454. https://doi.org/10.1007/s42241-019-0048-7.

Ji, L.L., Li, W., Shi, W.D., et al., 2020. Energy characteristics of mixed-flow pump under different tip clearances based on entropy production analysis. Energy 199, 117447. https://doi.org/10.1016/j.energy.2020.117447.

Ji, L.L., Li, W., Shi, W.D., et al., 2021. Effect of blade thickness on rotating stall of mixed-flow pump using entropy generation analysis. Energy 236, 121381. https://doi.org/10.1016/J.ENERGY.2021.121381.

Lee, J., Kim, Y., Khosronejad, A., et al., 2020. Experimental study of the wake characteristics of an axial flow hydrokinetic turbine at different tip speed ratios. Ocean Eng. 196, 106777. https://doi.org/10.1016/j.oceaneng.2019.106777.

Li, Y.J., Shen, J.F., Liu, Z.Q., et al., 2013. Large eddy simulation of unsteady flow in tip clearance of axial-flow pumps. Trans. Chin. Soc. Agric. Mach. 44 (S1), 113–118. https://doi.org/10.6041/j.issn.1000-1298.2013.S1.021 (in Chinese).

Li, B.W., Li, X.J., Jia, X.Q., et al., 2019. The role of blade sinusoidal tubercle trailing edge in a centrifugal pump with low specific speed. Processes 7 (9), 625. https://doi.org/10.3390/pr7090625.

Li, B., Lu, Q., Jiang, B.Y., et al., 2022. Effects of outer edge bending on the aerodynamic and noise characters of axial fan for air conditioners. Processes 10 (4), 686. https://doi.org/10.3390/PR10040686.

Li, W., Liu, M.J., Ji, L.L., et al., 2023. Study on the trajectory of tip leakage vortex and energy characteristics of mixed-flow pump under cavitation conditions. Ocean Eng. 267, 113225. https://doi.org/10.1016/j.oceaneng.2022.113225.

Ling, G.P., 2000. Research and development of oil-gas multiphase pump technology in China and abroad. J. East China Shipbuild. Inst. 14 (5), 83–87. https://doi.org/10.3969/j.issn.1673-4807.2000.05.019 (in Chinese).

Liu, C.Q., Gao, Y.S., Tian, S.L., et al., 2018. Rortex-A new vortex vector definition and vorticity tensor and vector decompositions. Phys. Fluids 30 (3), 35103. https://doi.org/10.1063/1.5023001.

Liu, M., Tan, L., Cao, S.L., 2019. Dynamic mode decomposition of gas-liquid flow in a rotodynamic multiphase pump. Renew. Energy 139, 1159–1175. https://doi.org/10.1016/j.renene.2019.03.015.

Long, Y., Zhou, Z., Li, N., et al., 2024. Experimental and numerical investigation of tip leakage vortex cavitation in water-jet pump. J. Appl. Fluid Mech. 17 (6), 1191–1203. https://doi.org/10.47176/jafm.17.6.2369.

Lu, H.J., Gao, S.T., 2003. On the helicity and helicity equations. Acta Meteorol. Sin. 61 (6), 684–691. https://doi.org/10.3321/j.issn:0577-6619.2003.06.005 (in Chinese).

Ma, R., Devenport, W.J., 2006. Unsteady periodic behavior of a disturbed tip-leakage flow. AIAA J. 44 (5), 1073–1086. https://doi.org/10.2514/1.12082.

Ma, R., Devenport, W.J., 2007. Tip gap effects on the unsteady behavior of a tip leakage vortex. AIAA J. 45 (7), 1713–1724. https://doi.org/10.2514/1.13536.

Muthanna, C., Devenport, J.W., 2004. Wake of a compressor cascade with tip gap, part 1: Mean flow and turbulence structure. AIAA J. 42 (11), 2320–2331. https://doi.org/10.47176/jafm.17.6.2369.

Nayak, A., Das, D., 2021. Experimental and numerical investigation of flow instability in a transient pipe flow. J. Fluid Mech. 920 (439), A39. https://doi.org/10.1017/JFM.2021.460.

Peng, D., Gregory, J.W., 2015. Vortex dynamics during blade-vortex interactions. Phys. Fluids 27 (5), 53104. https://doi.org/10.1063/1.4921449.

Rashidi, S., Hayatdavoodi, M., Esfahani, J.A., 2016. Vortex shedding suppression and wake control:a review. Ocean Eng. 126, 57–80. https://doi.org/10.1016/j.oceaneng.2016.08.031.

Scheeler, M.W., Reesm, V.W.M., Kedia, H., et al., 2017. Complete measurement of helicity and its dynamics in vortex tubes. Science 357 (6350), 487–491. https://doi.org/10.1126/science.aam6897.

Shen, X., Zhang, D.S., Xu, B., et al., 2021. Experimental and numerical investigation on the effect of tip leakage vortex induced cavitating flow on pressure fluctuation in an axial flow pump. Renew. Energy 163, 1195–1209. https://doi.org/10.1016/j.renene.2020.09.004, 2021.

o6.T0ExiaVC, 57Vq:6.TxtTt at V6fiwMKTMTMTfi6w.C:T7wfi6.T0fiq5fifi6w.C:Tw.fi6.KVCTK:6wf